Research Square

Preprints are preliminary reports that have not undergone peer review.
They should not be considered conclusive, used to inform clinical practice,
or referenced by the media as validated information.

Loading-Dependent Effects of J-AP on Polypropylene: Thermal Reinforcement and Electrostatic Charge Decay

Fatih Doğan
Çanakkale Onsekiz Mart University
Ayse Nur Ozkan
Manisa Celal Bayar University
Kamil Şirin
Manisa Celal Bayar University
İsmet Kaya
ikaya@comu.edu.tr

Çanakkale Onsekiz Mart University

Research Article

Keywords: Polypropylene, Polymer blends, Thermal degradation kinetics, Master plots, Electrostatic charge dissipation

Posted Date: October 30th, 2026

DOI: https://doi.org/10.21203/rs.3.rs-11372657/v1

License: This work is licensed under a Creative Commons Attribution 4.0 International License.
Read Full License

Additional Declarations: No competing interests reported.

Loading-Dependent Effects of J-AP on Polypropylene: Thermal Reinforcement and Electrostatic Charge Decay

Fatih Doğan[1], Ayse Nur Ozkan[2], Kamil Şirin[3], İsmet Kaya[4*]

[1]Faculty of Education, Secondary Science and Mathematics Education, Çanakkale Onsekiz Mart University, 17100, Çanakkale, Türkiye
[2]Applied Science Research Center, Manisa Celal Bayar University, Manisa, Türkiye
[3]Faculty of Engineering and Natural Sciences, Department of Chemistry, Manisa Celal Bayar University, Manisa, Türkiye
[4]Polymer Synthesis and Analysis Laboratory, Department of Chemistry, Faculty of Science, Çanakkale Onsekiz Mart University, 17020, Türkiye

Abstract

Polypropylene (PP) blends containing 0.5, 1.0, and 3.0 wt% poly(7-amino-4-hydroxy-2-naphthalenesulfonic acid) (J-AP) were prepared by twin-screw melt compounding to assess the effect of additive loading on their structural, thermal, morphological, mechanical, electrical, and electrostatic charge-dissipation properties. FTIR-ATR confirmed the incorporation of J-AP, while XRD revealed predominantly α-monoclinic crystalline structures. Increasing the J-AP content enhanced crystallinity and thermal stability: the DSC-derived crystallinity rose from 34.3% for neat PP to 45.4% for the 3.0 wt% blend, and the degradation onset temperature increased from 431 to 449 °C. The blends exhibited yellow fluorescence under 366 nm UV excitation, most pronounced at 3.0 wt% loading, and the elastic modulus increased from 456.1 MPa for neat PP to 1732.8 MPa for the 3.0 wt% blend. Thermal degradation kinetics were evaluated by six methods at four heating rates (5, 10, 15, and 20 °C min^{-1}); all indicated higher apparent activation energies after J-AP incorporation. Experimental master plots agreed most closely with the D2 diffusion model for the 0.5 and 1.0 wt% blends and with the D1 model for the 3.0 wt% blend. Electrical conductivity increased from 7.6×10^{-10} to 1.7×10^{-9} S cm^{-1} across the series. However, corona-induced charge-decay measurements showed that higher conductivity did not translate into faster charge dissipation: the 0.5 wt% blend gave the shortest decay times under both positive and negative polarization, although its ESD performance remained limited. These results identify J-AP as a multifunctional PP modifier with distinct loading requirements for thermal-mechanical enhancement and electrostatic charge dissipation.

Keywords: Polypropylene, Polymer blends, Thermal degradation kinetics, Master plots, Electrostatic charge dissipation.

Correspondence to: ikaya@comu.edu.tr; Phone: +90 286 2180018 Fax:+90 286 2183917

Introduction

Polyolefins, particularly polypropylene (PP), are cornerstone materials in numerous industrial applications ranging from advanced packaging to automotive and electronic components. Their widespread utilization is attributed to their excellent chemical resistance, favorable mechanical properties, and outstanding processability **[1]**. However, neat PP possesses inherently high surface electrical resistivity. This highly insulating nature leads to the undesirable accumulation of static charges, which causes significant handling difficulties and poses critical electrostatic discharge (ESD) hazards in manufacturing and consumer uses **[2]**. To overcome these limitations, imparting electrical conductivity to polymers that are otherwise insulating has become a significant research area. Polymeric materials that have acquired conductive properties are extensively utilized across a broad spectrum of advanced engineering applications. These include electromagnetic interference (EMI) shielding, flexible electronics, wearable sensors, antistatic packaging, and corrosion-resistant coatings **[3,4]**. In these critical applications, the ability to safely dissipate static electricity or conduct electrical signals is just as important as maintaining the mechanical integrity of the host matrix.

A variety of conductive fillers have been investigated to impart electrical conductivity to insulating polyolefins. These approaches commonly involve carbonaceous nanofillers, such as carbon nanotubes (CNTs), graphene, and reduced graphene oxide (rGO), as well as metallic nanoparticles and networks **[5,6]**. However, depending on filler chemistry, loading, and processing conditions, these systems may exhibit poor interfacial adhesion, agglomeration, and reduced processability or flexibility **[7]**. Blending polyolefins with intrinsically conducting polymers (ICPs), such as polyaniline (PANI), polypyrrole (PPy), and polythiophene (PTh), offers another approach to modifying their electrical properties. The tunable chemical structures of ICPs provide opportunities to tailor interactions with the host matrix, although their compatibility and dispersion depend on the polymer chemistry, additive loading, and processing conditions **[8]**.

In recent years, numerous research groups have investigated polymer composites containing conductive phases. Takahashi et al. **[9]** optimized the thermal doping temperature of polyaniline and the radical polymerization temperature to develop a solvent-free thermosetting resin composite with an electrical conductivity of 1.45 S cm^{-1}. Silva et al. **[10]** developed an antistatic packaging material by melt-extruding a blend of recycled PET, PC, and cobalt-doped polyaniline, reporting a resistivity of 0.42×10^{8} Ω m. Mohsin et al. **[11]** investigated the electrical, thermal, and rheological properties of grafted polypyrrole/polypropylene blends, highlighting their potential for electrostatic charge dissipation. Anis et al. **[12]** prepared a

mouldable conductive thermoplastic composite incorporating polythiophene derivatives, demonstrating electrical conductivity while maintaining processability. Building on these studies, the present work explores poly(7-amino-4-hydroxy-2-naphthalenesulfonic acid) (J-AP) as an alternative functional modifier for polypropylene (PP). Particular attention is given to whether changes in electrical conductivity are accompanied by corresponding changes in electrostatic charge dissipation and how these effects relate to the structural and thermal-mechanical properties of the blends.

Accordingly, PP blends containing 0.5, 1.0, and 3.0 wt% J-AP were prepared by twin-screw melt compounding. The effects of J-AP loading on their structural, thermal, morphological, mechanical, and electrical properties were systematically investigated. Surface potential decay following positive and negative corona charging at ±3, ±5, and ±7 kV was evaluated using the 1/e decay time and the 10% cut-off time. This approach enabled an assessment of the balance between thermal-mechanical performance and electrostatic charge dissipation across the investigated compositions.

Preparation of Blends

The binary blends were synthesized via melt-processing in a twin-screw microextruder at a processing temperature of 210 °C. To ensure a high degree of macromolecular integration, the neat polypropylene (PP) matrix was loaded with J-AP, Poly (7-amino-4-hidroksi-2-naftalensülfonik asit) at mass fractions of 0.5%, 1%, and 3%, maintaining a constant rotor speed of 60 rpm for a residence time of approximately 45 minutes. For each composition, a total of 4 g of PP was processed under standardized extrusion parameters. The resulting composites were designated as $PJ_{0.5}$, PJ_1, and PJ_3, corresponding to their respective J-AP loading levels. The intrinsic conductivity of J-AP and its blends was measured in solid pellet form under a hydraulic pressure of 1600 kg/cm². Accordingly, the self-doped conductivity of J-AP was determined to be approximately 10^{-3} S cm^{-1}. Subsequently, the surface conductivities of the blend films were characterized using a Keithley 2400 electrometer under identical experimental conditions. The measured values were 7.6 10^{-10} S/cm^{-1} for $PJ_{0.5}$, 8.7 10^{-10} S/cm^{-1} for PJ_1, and 1.7 10^{-9} S/cm^{-1} for PJ_3. A definitive upward trend in conductivity was observed in correlation with the increasing filler concentration. These findings suggest that the J-AP additive achieved a homogeneous distribution and an excellent state of dispersion within the PP matrix and a finding that is also confirmed by SEM analysis. Effective antistatic performance in polyolefin-based systems is characterized by a conductivity window of 10^{-6}-10^{-11} Scm^{-1} **[13]**. Given that our PJ_n blends demonstrate surface conductivities strictly within this interval, they can be categorized as highly suitable candidates for high-performance antistatic materials.

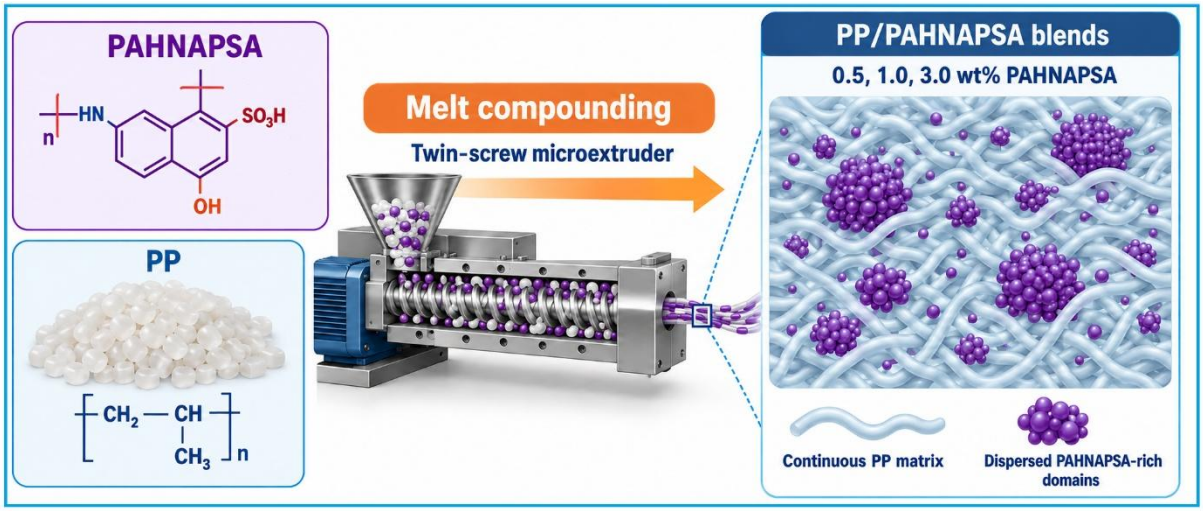
Experimental

Materials

Polypropylene (PP) used in this study was the commercial grade PETOPLEN FH250, supplied by Petkim Petrochemical Company (Aliağa, İzmir, Türkiye). PETOPLEN FH250 is a polypropylene homopolymer with a medium molecular mass distribution, developed primarily for biaxially oriented polypropylene (BOPP) film applications. According to the supplier's technical data sheet, the resin has a melt flow rate of 2.5 g 10 min^{-1}, measured at 230 °C under a load of 2.16 kg, and a density of 0.905 g/cm^3. Its melting temperature, determined by differential scanning calorimetry (DSC) during the second heating cycle, is 160 °C. These characteristics establish the identity and baseline processing properties of the PP matrix used to prepare the blends investigated in this study. The supplier reports a tensile strength at yield of 35 MPa and a flexural modulus of 1350 MPa at 23 °C. The notched Izod impact strength is 40 J m^{-1} at 23 °C, while the Rockwell hardness is 93 on the R scale. The reported heat deflection temperature is 82 °C under a stress of 0.45 MPa. Together, these typical values provide a reference for assessing changes in mechanical and thermal behavior after the incorporation of the modifier. The mechanical properties reported by the supplier were measured using compression molded sheets and should therefore be distinguished from measurements performed on the blends prepared in this study. For film extrusion, the recommended processing conditions comprise typical zone temperatures of 220-250 °C and a die head temperature of 250 °C. The actual processing conditions used to prepare the PP blends were selected according to the experimental procedure described below. Unless otherwise stated, the properties listed in this paragraph refer to the neat PETOPLEN FH250 resin rather than to the resulting blends. 7-Amino-4-hydroxy-2-naphthalenesulfonic acid [synonym: (J-acid), acronym: AHNAPSA; 99%, ACS reagent], sodium hypochlorite, hydrogen peroxide (30% w/w aqueous solution), potassium hydroxide (≥85%, ACS reagent, pellets), hydrochloric acid (37%, AR grade), and all other chemicals were supplied by Sigma-Aldrich Chemical Company (Germany). Poly (7-amino-4-hydroxy-2-naphthalenesulfonic acid) (PAHNAPSA, J-AP) was synthesized by oxidative polymerization of AHNAPSA following the procedure reported by Doğan et al. **[14]** . Horseradish peroxidase (HRP) was also purchased from Sigma-Aldrich as a solid powder (259 purpurogallin units/mg solid; RZ = 3.0). It was used to catalyze the polymerization of AHNAPSA in a dioxane/sodium phosphate buffer mixture at room temperature.

J-AP was incorporated into the PP matrix at concentrations of 0.5, 1.0, and 3.0 wt % by melt compounding in a twin-screw microextruder. The J-AP loadings of 0.5, 1.0, and 3.0 wt% were calculated based on the total mass of each blend (PP + J-AP). The resulting blends were

examined to determine how J-AP loading affected their morphology, thermal behavior, physical and mechanical properties, electrical properties, and antistatic performance. The blend preparation procedure is illustrated in **Scheme 1**.



Scheme 1. Schematic illustration of the preparation of PP/PAHNAPSA blends by twin-screw melt compounding at PAHNAPSA loadings of 0.5, 1.0, and 3.0 wt%. The enlarged view conceptually depicts PAHNAPSA-rich regions dispersed within the continuous PP matrix

Techniques

The prepared blends were examined by Fourier transform infrared spectroscopy using a PerkinElmer Frontier FT-IR/FIR/MIR spectrometer. Spectra were acquired from film samples at room temperature with a PIKE Technologies Gladi ATR accessory over the range 4000-400 cm^{-1}. Thermal properties were evaluated by thermogravimetric analysis (TGA) on a PerkinElmer Diamond Thermal Analyzer and differential scanning calorimetry (DSC) on a PerkinElmer Pyris Sapphire instrument. For DSC, samples weighing 8-10 mg were heated from 25 to 400 °C at 10 °C min^{-1} under nitrogen flowing at 100 mL min^{-1}. TG-DTA measurements were performed with 5-10 mg samples in platinum crucibles. Under a nitrogen flow of 200 mL min^{-1}, the samples were heated from 25 to 700 °C at rates of 5, 10, 15, and 20 °C min^{-1}. Solid-state electrical conductivity was measured by the four-point probe method using a Keithley 2400 electrometer. Dynamic mechanical analysis (DMA) was conducted in single cantilever mode with a PerkinElmer Pyris Diamond DMA 115 V instrument. The samples were heated from 20 to 350 °C at 3 °C min^{-1} under a nitrogen flow of 100 mL min^{-1}. Blend surface morphology was investigated using a JEOL JSM-7100F Schottky field emission scanning electron microscope (FE-SEM). Surface topography and three-dimensional features were further examined by atomic force microscopy (AFM; Alpha 300 A, WITec, Ulm, Germany). X-ray diffraction (XRD) patterns were obtained with a PANalytical Empyrean diffractometer

using Cu Kα radiation (λ = 1.54 Å). Data were collected over a 2θ range of 5°–90° at a scan rate of 4° min^{-1}.

Result and discussion

FTIR-ATR Spectra of J-AP-Modified PP Blends

Fig.1 presents the FTIR-ATR spectra of PP blends containing different concentrations of J-AP. The FTIR spectra of the J-AP-doped PP blends, illustrated in **Fig. 1**, exhibit characteristic absorption bands at 2976 cm^{-1} and 2871 cm^{-1}, corresponding to the asymmetric and symmetric -CH_2 stretching vibrations, respectively. The peaks observed at 1464 $cm^{-1}$and 1369 $cm^{-1}$are attributed to the -CH_3 asymmetric stretching and -CH_3 symmetric deformation vibrations. Furthermore, the band at 1173 cm^{-1} is identified as -CH vibrations, while the absorption features at 998, 973, 846, and 807 $cm^{-1}$are assigned to the -CH and -CH_2 rocking vibration modes. In addition to the PP signals, the successful integration of the dopant is confirmed by the bands at 1146 and 1053 cm^{-1} which are attributed to the symmetric and asymmetric stretching vibrations of the sulfonyl groups within the J-AP structure. Notably, a broad band detected at 3342 cm^{-1} was identified as originating from the UV stabilizers present in the formulation.

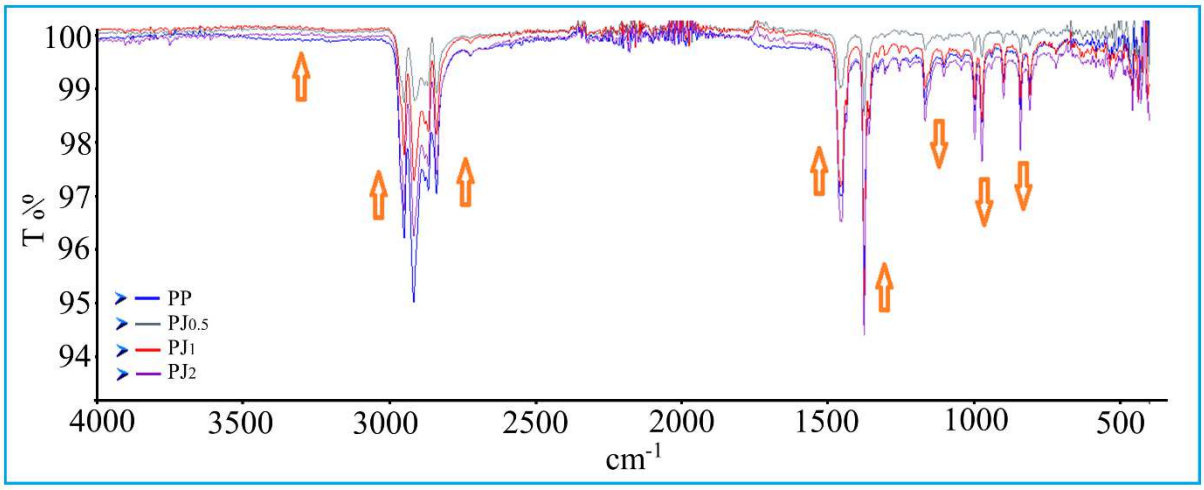


Fig. 1. FTIR spectra of J-AP doped PP blends.

Solid-State Fluorescence Properties of J-AP-Doped PP Blends

The solid-state fluorescence properties of the PJ_n coded blends were examined under UV excitation at 366 nm at room temperature. The visible emission colors generated

by each blend were photographically recorded. **Fig. 2** presents the images of the neat PP and the J-AP-doped PJ_3 blend under UV illumination at 366 nm. Upon the incorporation of the target material into the PP matrix, the resulting blends exhibited a characteristic yellow emission. The most distinct visual fluorescence was achieved in the PJ_3 blend. Consequently, fluorescent properties were successfully imparted to the PP matrices through the utilization of the J-AP target material.

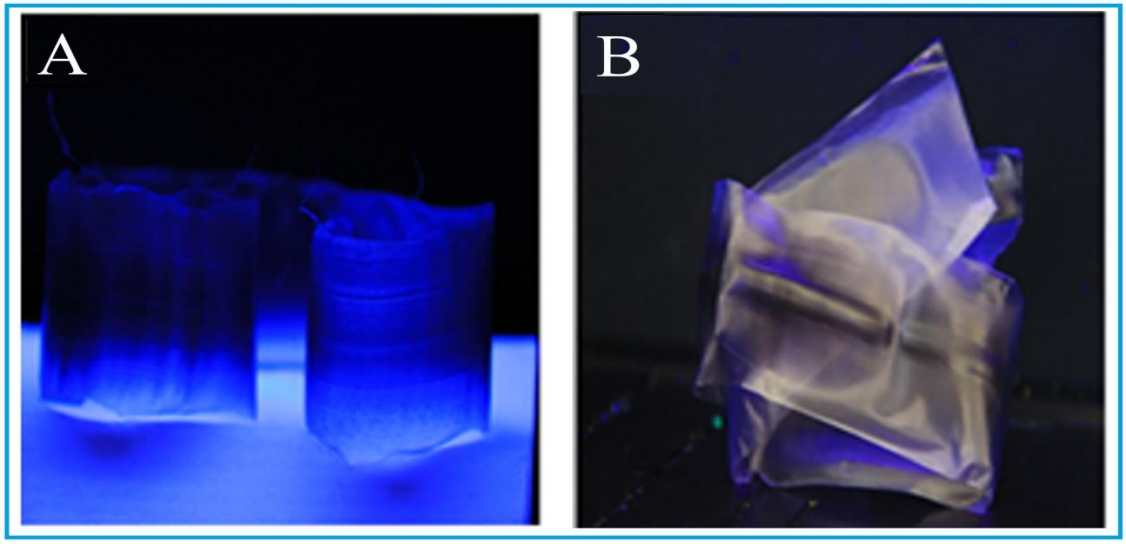


Fig. 2. Images of neat PP (A) and PJ_3 (B) blends under UV light.

TG/DTG-DTA-DSC curves of J-AP-Doped PP Blends

The TG/DTG-DTA and DSC curves of the J-AP doped PP blends are illustrated in **Fig. 3**. **Fig. 3(A)** reveal that both the neat PP and the PJ_n blends undergo a single-step thermal degradation process. The onset decomposition temperatures were recorded as 431 °C, 438 °C, 445 °C, and 449 °C for the neat PP, $PJ_{0.5}$, PJ_1, and PJ_3 blends, respectively. It is evident that as the J-AP dopant concentration increases, the decomposition onset temperature shifts to higher values, indicating a significant enhancement in the thermal stability of the PP matrix. In the DTA curves, the endothermic events observed at approximately 164 °C and 442 °C were attributed to the melting point and the decomposition reaction of the neat PP, respectively. However, the Vicat softening point of the neat PP could not be detected in the DTA curves of the PJ_n blends. From the DTG curves, the temperatures corresponding to the maximum degradation rate were determined as 442 °C, 448 °C, 451 °C, and 453 °C for the neat PP, $PJ_{0.5}$, PJ_1, and PJ_3 blends, respectively. Consequently, the progressive

addition of the J-AP polymer to the PP matrices systematically shifts the onset of decomposition to higher temperatures, thereby improving their overall thermal stability.

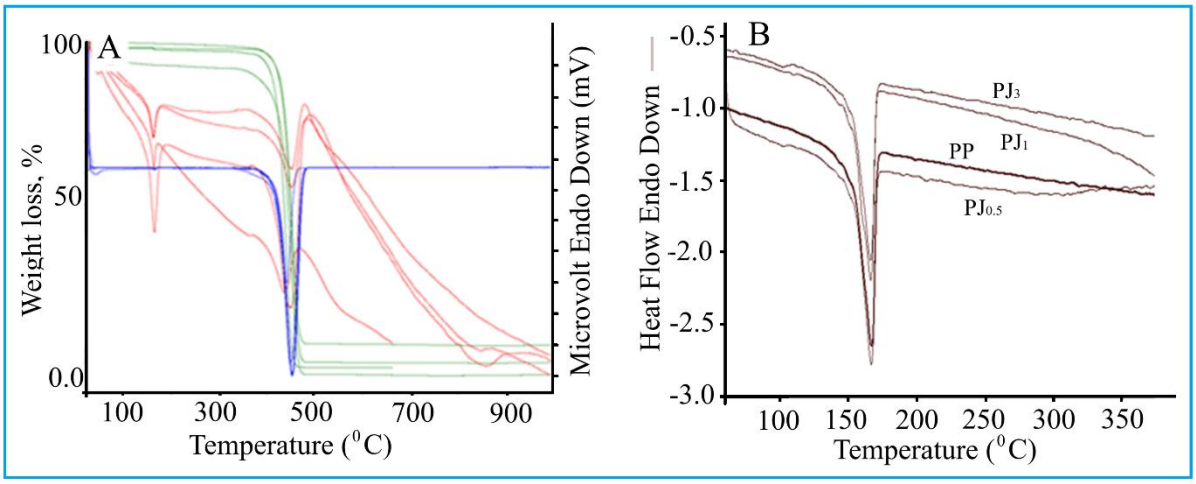


Fig. 3. TG/DTG-DTA (A) and DSC (B) curves of the J-AP-doped PP blends.

Fig. 3 (B) presents the DSC curves of the J-AP-doped PP blends. According to the literature, the deformation temperature (α -transition) and the melting point of neat PP are typically observed at approximately 114 °C and 160 °C, respectively. As depicted in **Fig. 3**, the curve of the neat PP (indicated by the bold line) did not exhibit a distinct deformation temperature, displaying only a melting peak at around 157 °C. Furthermore, in the PJ_n blends, endothermic effects attributed to the dehydration reactions of the J-AP polymer were detected at 138 °C and 100 °C. Moreover, it was found that increasing the concentration of the J-AP dopant within the neat PP matrix led to an increase in both the melting temperature and the degree of crystallinity for the PJ_n blends. Additionally, the deformation temperature disappeared in all PJ_n blends, while the melting point and crystallization temperatures generally shifted to higher values in correlation with the increasing mass fraction of the additive. The DSC data are given in **Table 1**.

Table 1. DSC, X-RD and FT-IR data of neat PP and PJ_n blends.

	T_{onset}, °C	$T_{melting}$, °C	T_{end}, °C	T_{Chris}, °C	ΔH, j/g	Xc^d, %	Xc^R, %	Xc^F, %
PP	153.7	157.0	172.3	127.6	71.7	34.3	24.7	28.1
$PJ_{0.5}$	157.6	159.3	170.1	131.8	72.3	36.9	39.2	30.8
PJ_1	158.2	163.1	169.9	132.1	79.4	39.5	40.8	31.4

PJ_3	159.6	166.7	168.3	133.8	89.1	45.4	41.3	32.9

The degree of crystallinity was calculated using three different techniques: DSC (Xc^d), XRD (Xc^R), and FTIR (Xc^F)

X-ray Diffraction (XRD) Patterns of the J-AP-Doped PP Blends

Fig. 4 displays the X-ray diffraction (XRD) patterns of neat PP and PJ_n blends. Commercial polypropylenes typically exist in polymorphic or mesomorphic architectures comprising α, β, γ crystalline phases **[15]**. Building upon this framework, the X-ray diffraction patterns of the neat PP and the PJn blends revealed that the neat PP utilized in this study constitutes a polymorphic system, characterized by both α and β crystal structures along with their corresponding unit cells. As is well established in the literature, the macroscopic morphology of the polymer is fundamentally dictated by the predominant crystalline formations within the neat PP matrix **[16]**. Regarding the PJ_n series, the $PJ_{0.5}$, PJ_1, and PJ_3 blends were observed to crystallize in the monoclinic α -form. Variations in specific parameters, such as cross-linking, blend formation, or oxidation, can induce phase transitions among different crystalline architectures **[17]**. Consequently, these findings indicate that the incorporation of the J-AP target particles effectively enhances the degree of crystallinity of the neat PP.

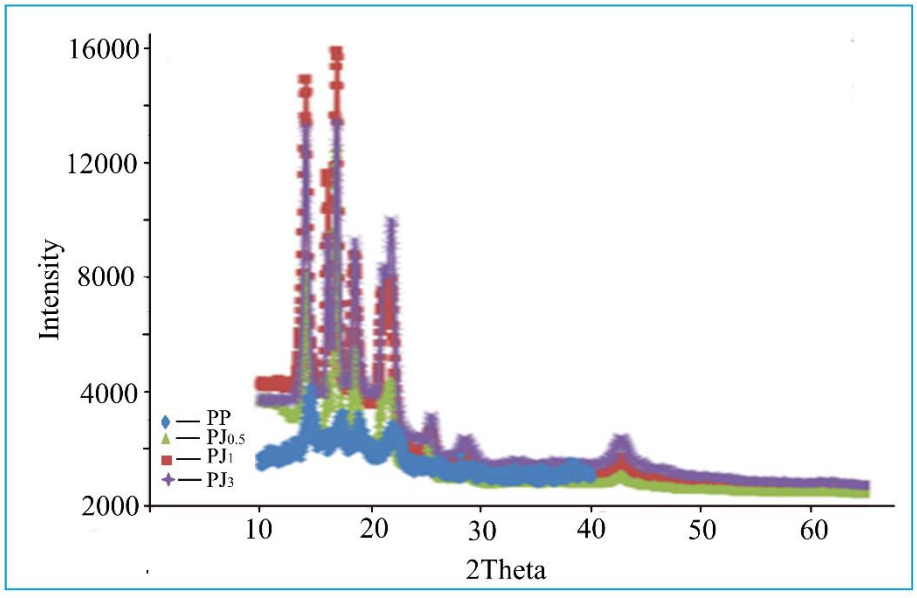


Fig. 4. X-ray diffraction (XRD) patterns of the neat PP and the PJ_n blends.

DMA Curves of the J-AP-Doped PP Blends

Fig. 5 presents DMA curves of the neat PP and the PJ_n blends. Based on these profiles (**Fig. 5A**), the deformation temperature (α-transition) of the neat PP, which remained

undetected in the DSC curves, was identified at 118 °C, while the melting point was determined to be 151 °C. This melting point is in good agreement with the prior DSC findings. Furthermore, it was established that the neat PP predominantly exhibits nonlinear viscous behavior. An evaluation of the DMA curves also revealed a progressive decline in both the storage and loss modulus as a function of temperature, which is directly attributed to the enhanced segmental mobility of the polymer chains. The DMA curves corresponding to the $PJ_{0.5}$ (B), PJ_1 (C), and PJ_3 (D) blends are presented in **Fig. 5**. From these curves, the deformation temperatures originating from the neat PP matrix were recorded as 116.6 °C, 118.7 °C, and 119.8 °C for the $PJ_{0.5}$, PJ_1, and PJ_3 blends, respectively. Concurrently, their melting points were determined as 163.3 °C, 168.7 °C, and 171.9 °C, respectively. Furthermore, the decomposition temperatures of the J-AP particles within the PJ_n blends were identified as 171.4 °C, 176.2 °C, and 179.2 °C for the $PJ_{0.5}$, PJ_1, and PJ_3 blends, respectively. Overall, it was found that an increase in the loading level of the J-AP particles within the neat PP matrix led to a systematic elevation in both the deformation and melting temperatures across all blends.

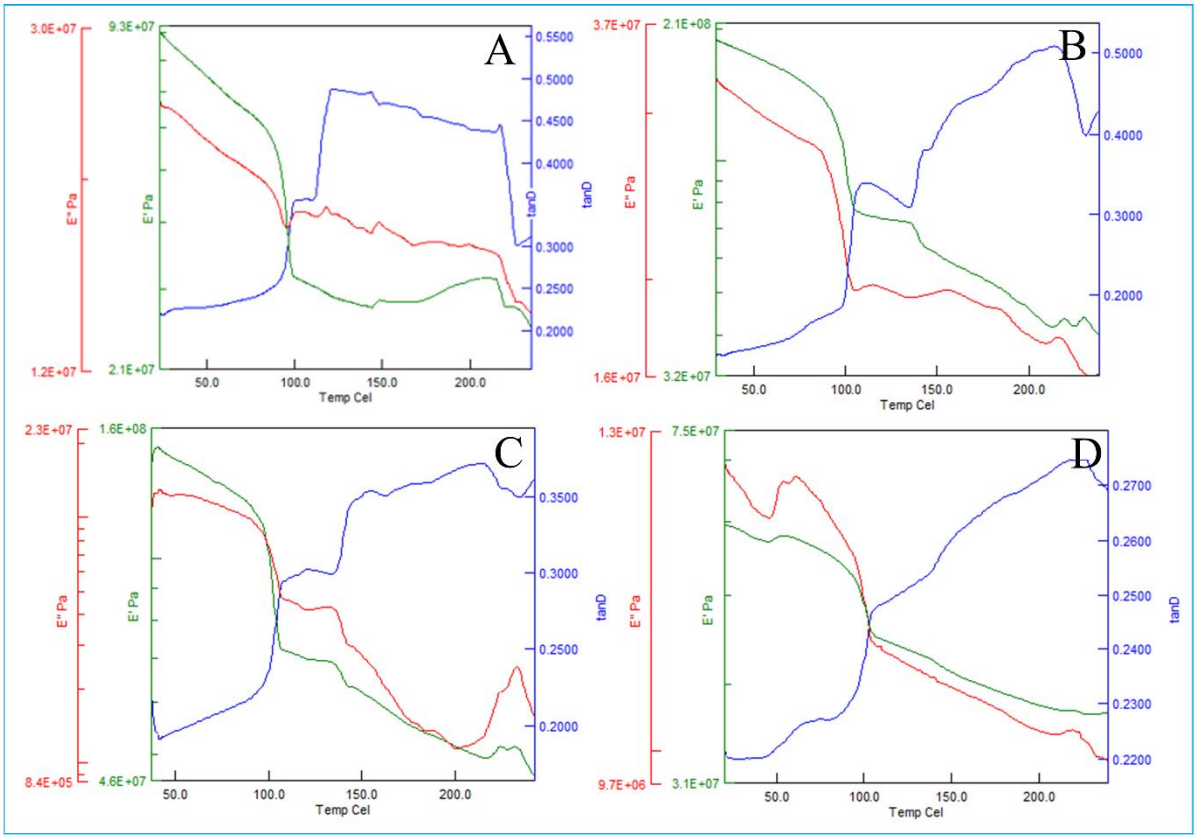


Fig. 5. DMA curves of neat PP (A), $PJ_{0.5}$ (B), PJ_1(C) and PJ_3 (D) blends.

In the DMA curves illustrating the temperature dependence of the storage modulus for the PJ_n blends, distinct regions were identified: the deformation phase, the melting phase of the PP matrix, the decomposition phase of the J-AP particles, and the dispersion region. At low temperatures, the storage modulus of the neat PP and the PJ_n blends were observed to be nearly identical, indicating that the incorporation of J-AP particles does not significantly contribute to the stiffness of the PP matrix in this temperature regime. However, at elevated temperatures, an increase in the dopant concentration led to a systematic enhancement in all modulus of the PJ_n blends, thereby increasing their overall stiffness relative to the neat PP. It was determined that this outcome is closely correlated with the degree of crystallinity, which is consistent with observations in other blend systems. Furthermore, the doped PJ_n blends were also found to exhibit nonlinear viscous behavior.

SEM Images of the J-AP-Doped PP Blends

Fig. 6 displays SEM images of the neat PP and the PJ_n blends. Morphological observations reveal that the neat PP films exhibit a smooth surface topography (**Fig. 6A**). As evidenced by the SEM micrograph of the $PJ_{0.5}$ blend, the J-AP polymer demonstrated excellent dispersion within the PP matrix across different phases at a low loading level. The abundant dispersed nodules observed on the surface possess dimensions of approximately 30 nm. In the PJ_1 blend, t ogether with the appearance of different crystalline zones on the surface, it is seen that the J-AP polymer exhibits a relatively good dispersion with the neat PP. Furthermore, distinct crystalline channels were observed on the surface of the PJ_3 blend, alongside an excellent dispersion between the J-AP polymer and the neat PP. The nodule sizes in the PJ_3 blend were found to be significantly smaller (5 nm) compared to those in the $PJ_{0.5}$ and PJ_1 blends. The overall film thicknesses of the $PJ_{0.5}$, PJ_1, and PJ_3 blends range from 50 to 900 μm

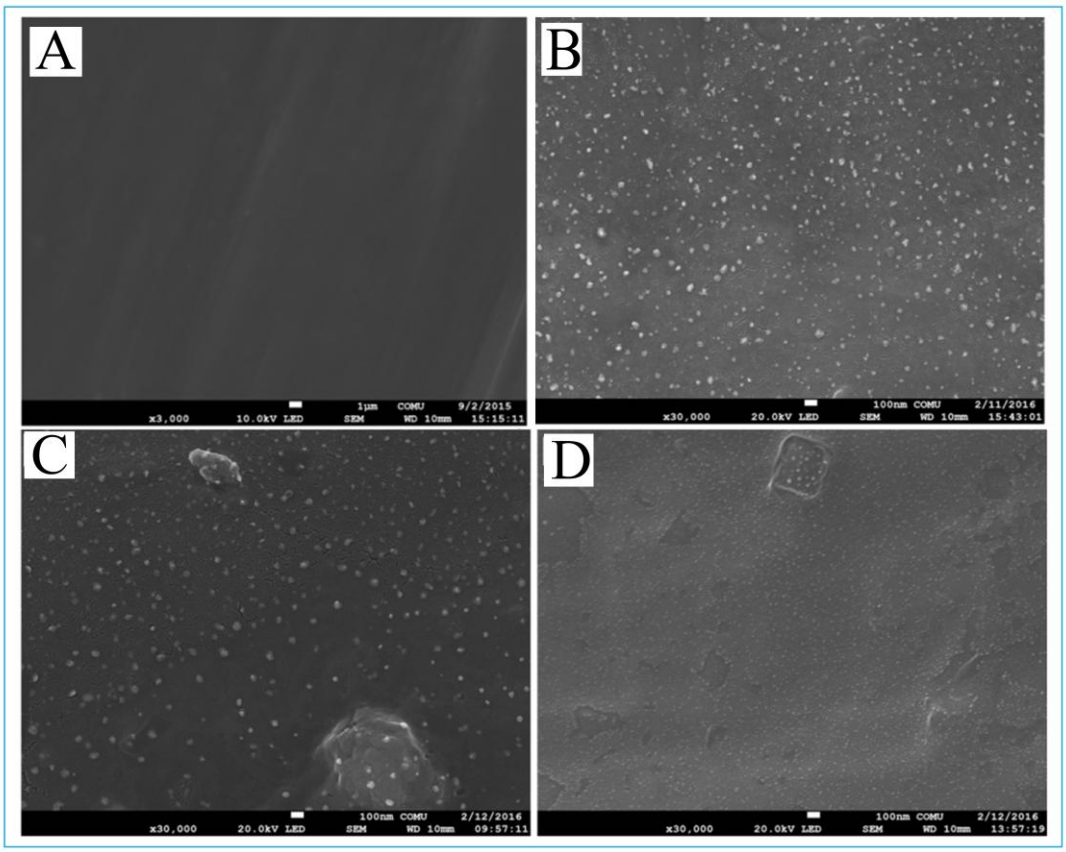


Fig. 6. SEM images of the neat PP(A), $PJ_{0.5}$(B), PJ_1(C) and PJ_3(D) blends.

AFM Images of the J-AP-Doped PP Blends

High-resolution, three-dimensional topographical images of the blend surfaces were acquired utilizing AFM. Furthermore, the surface morphology of the synthesized blends and the influence of the dopant incorporation on the surface roughness were investigated via these AFM micrographs. The surface roughness was quantitatively evaluated using the Ra (arithmetic average roughness) and RMS (root mean square roughness) parameters. While Ra is predominantly utilized as a roughness parameter for quality control purposes, the RMS value represents the standard deviation of the surface height distribution. Consequently, surface roughness is considered a critical parameter in statistical evaluations **[18]**. **Fig. 7(A)** presents the three-dimensional AFM images of the neat PP. Based on these topographies, the RMS and Ra values of the neat PP film were measured at 39.57 nm and 29.80 nm, respectively. The acquired data indicate a proportional relationship between the RMS and Ra values of the neat PP film. Additionally, the surface of the neat PP was observed to be inherently uneven and rough. Moreover, the average nodule size for the neat PP was determined to be 390.43 nm. This morphological characteristic was attributed to the presence of varying polymer chain lengths resulting from different degrees of polymerization. **Fig. 7 (B-D)** presents the three-dimensional

AFM images of the $PJ_{0.5}$, PJ_1, and PJ_3 blends. According to these images, the RMS values of the $PJ_{0.5}$, PJ_1, and PJ_3 films were measured at 26.12 nm, 29.96 nm, and 51.75 nm, respectively, while their corresponding Ra values were determined to be 19.90 nm, 22.64 nm, and 40.99 nm, respectively. The obtained results indicate a proportional relationship between the RMS and Ra values across the $PJ_{0.5}$, PJ_1, and PJ_3 films. Additionally, the surfaces of the PJ_n blends exhibit an inherently uneven and rough topography. Moreover, the average nodule sizes for the $PJ_{0.5}$, PJ_1, and PJ_3 blends were recorded as 115.84 nm, 134.43 nm, and 193.39 nm, respectively. Ultimately, these findings demonstrate that J-AP incorporation reduced surface roughness at 0.5 and 1.0 wt%, whereas the 3.0 wt% blend exhibited higher roughness than neat PP.

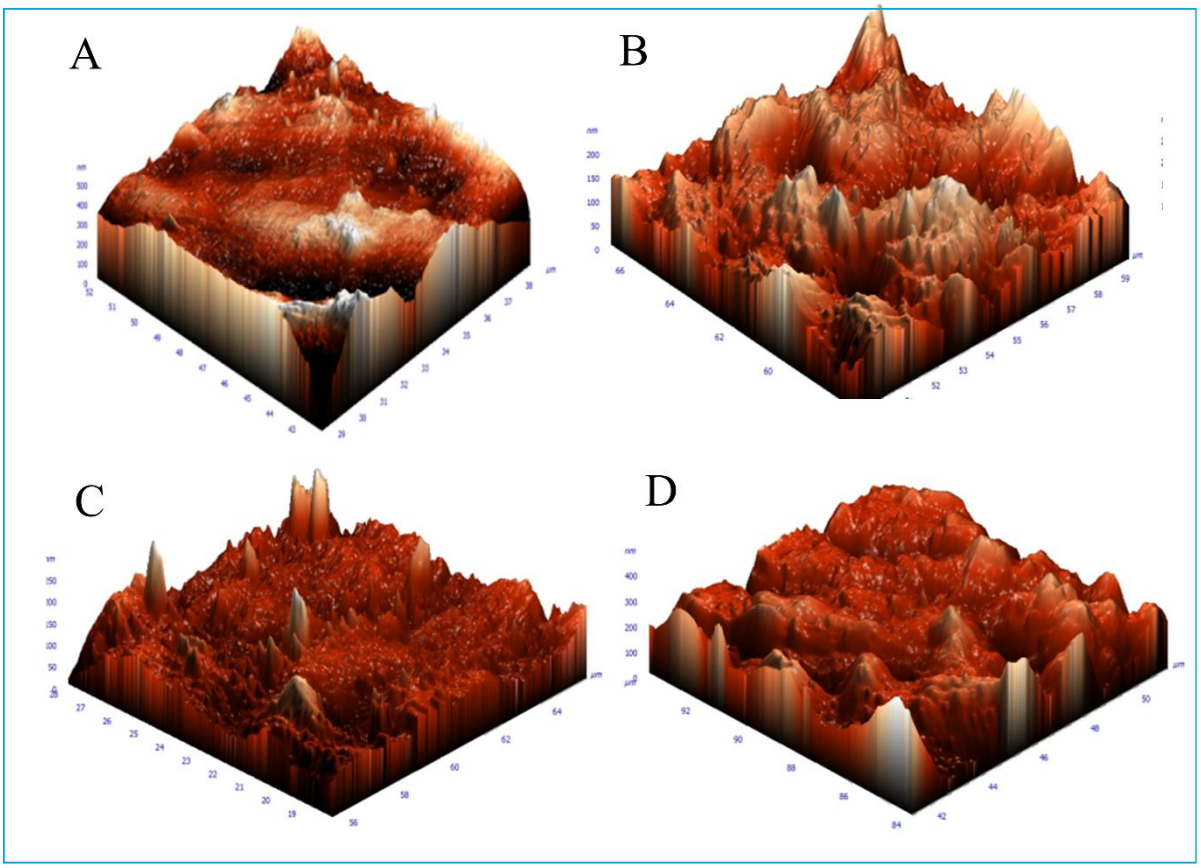


Fig. 7. AFM images of neat PP(A), $PJ_{0.5}$ (B), PJ_1(C) and PJ_3 (D) blends.

Physicomechanical Properties of the J-AP-Doped PP Blends

The tensile properties of neat PP and its blends were evaluated using a Zwick Roell Z-250 testing machine in accordance with ASTM D638. The resulting stress–strain curves were used to determine Young's modulus, tensile strength, and elongation at break, providing insight into the effects of blend composition on stiffness, strength, and ductility. The stress-strain curve of the neat PP is given in **Fig. 8 (A)**. According to this, PP exhibited an elastic deformation region,

a homogeneous plastic deformation region, and a non-homogeneous plastic deformation region. The modulus of elasticity of the neat PP was found as 456.1 MPa. In this case, neat PP is more rigid due to its chemical composition and shows less shape change with stress. Also, the high bond energy between atoms and high melting temperature prove the high modulus of elasticity of neat PP. In case stresses are applied above the yield strength, which expresses the resistance of materials, plastic shape changes (permanent-irreversible) begin. According to this, in the plastic shape change region of PP, first homogeneous plastic shape changes after the yield point (yield strength for PP is 12.8 MPa) and heterogeneous plastic shape changes after the max point (tensile strength for PP is 13.6 MPa) were observed. The breaking strengths of the neat PP is determined as 12.35 MPa. Additionally, the elongations at yield and at break for the neat PP were found to be 5.76% and 262.18%, respectively. The stress-strain curves of the PJ_n blends are given in **Fig. 8 (B)**. According to this, almost all blends exhibited typical stress-strain curves specific to semi-crystalline polymers. In such graphs, the slopes of the strain curves being positive originates from the increase of its crystallinity as a result of the structural arrangement of the polymer with the increase in the amount of applied load. It is another important result that these improvements in question for neat PP show parallelism with the percentage amounts of the target materials.

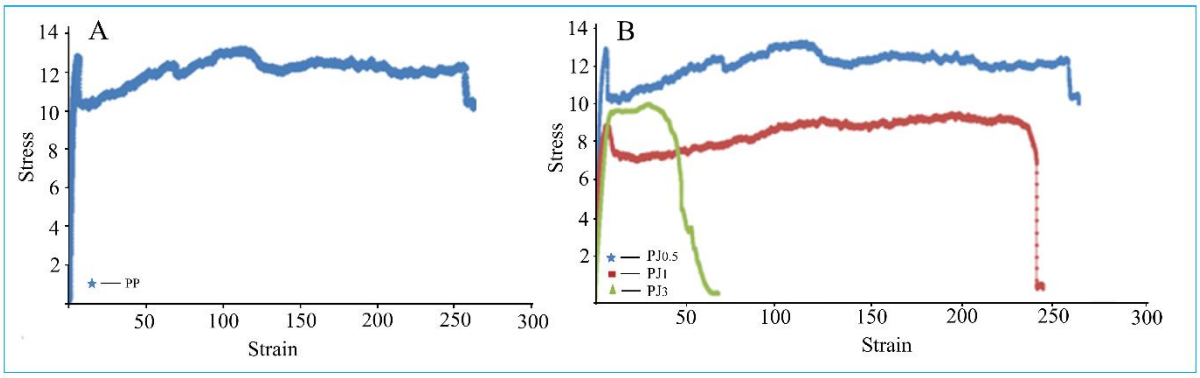


Fig. 8. Stress-strain curve of neat PP (A) and PJ_n blends (B).

The elastic moduli of $PJ_{0.5}$, PJ_1, and PJ_3 were 663.7, 529.4, and 1732.8 MPa, respectively, indicating a nonmonotonic dependence on J-AP loading. PJ_3 exhibited the highest elastic modulus, corresponding to an increase of approximately 279.9% relative to neat PP (456.1 MPa). This increase in stiffness may be associated with the higher crystallinity indicated by DSC and XRD analyses. The tensile strengths and stresses at break were 14.36 and 12.1 MPa for $PJ_{0.5}$, 10.61 and 9.3 MPa for PJ_1, and 10.56 and 8.7 MPa for PJ_3, respectively. The corresponding yield strengths were 12.41, 9.68, and 9.5 MPa. The elongations at yield and at

break were 5.23% and 268.2% for $PJ_{0.5}$, 5.38% and 248.17% for PJ_1, and 7.72% and 73.58% for PJ_3, respectively.

Electrostatic Discharge Behavior of neat PP

While the developments in the electronics industry continue rapidly, they bring many problems together with them. Without a doubt, the most important of these problems is electrostatic discharge (electrostatic charge dissipation, ESD). The damages given by ESD are not to be underestimated at all. Today, it has been determined that these damages are ESD-sourced at a rate of 25% in electronic materials and 50% in working devices. Along with this, the importance of this problem has been understood much better recently and the studies done to eliminate the problem have gained speed in the last years. These studies presented in the literature primarily propose ESD protection by incorporating semiconducting dopants into the base materials utilized in the electronics industry. Consequently, the semiconductivity threshold for the materials to be employed as additives has been established within the range of 10^{-6} -10^{-11} $S.cm^{-1}$. Furthermore, it has been noted that the antistatic (ESD) protection performance is fundamentally dependent on both the morphology and the mass fraction of the incorporated dopants. Building upon this premise, the intrinsic conductivity (undoped/self-doped) of the J-AP polymer utilized in this study was recorded as 1.10^{-3} Scm^{-1}. As articulated in the research proposal, this result demonstrates the viability of utilizing polydisulfoaminonaphthol polymers as effective ESD materials. The ESD applications of the J-AP polymers dispersed within the neat PP matrix were evaluated using a Static Decay Meter (Model 406D, Electro-tech Systems, USA) and a Charge Decay Time Analyser (JCI 155v6, John Chubb Instrumentation, UK). These tests aimed to determine the dissipation times of the static charges accumulated on the surfaces of the neat PP and the blends following variations in the applied corona voltage. Accordingly, the charge dissipation profiles for the neat PP and PJ_n blends were digitally recorded via the corresponding software. The measurements were conducted at room temperature under various applied positive (3, 5, and 7 kV) and negative (-3, -5, and -7 kV) corona voltages on the material surfaces. **Fig. 9** presents the electrostatic discharge curve of the neat PP.

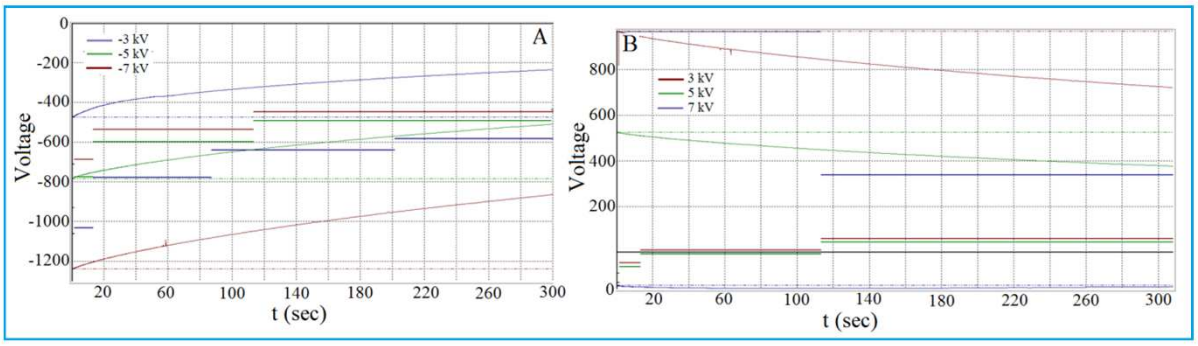


Fig. 9. Electrostatic discharge curves of neat PP at -3, -5 and -7 kV (A) and 3, 5 and 7 kV (B) corona voltages.

Fig. 9 illustrates the JCI curves of the neat PP under applied corona voltages of -3, -5, and -7 kV, as well as 3, 5, and 7 kV. As evidenced by these curves, the surface of the neat PP accommodates substantially high surface voltages under elevated negative and positive polarizations. However, the dissipation times for the static charges accumulated on the neat PP surface could not be measured within the extended observation window (up to 300 seconds). The quantitative results derived from these measurements are summarized in **Table 2**.

Table 2. ESD values of the neat PP at different corona voltages.

Corona voltage	Corona time	Surface humidity	Surface temperature	Surface voltage	1/e time	%10 Cut-off time	Surface charge	Capacitance
-7000	0.030	32.8	28.5	-1293.6	nd	nd	-19.84	9.652
-5000	0.030	32.8	28.2	-822.10	nd	nd	-11.32	6.693
-3000	0.007	32.9	28.5	-484.20	nd	nd	-2.630	1.512
3000	0.009	32.8	28.2	-726.10	nd	nd	4.480	1.982
5000	0.030	32.8	28.2	527.6	nd	nd	9.280	3.418
7000	0.030	32.7	28.5	969.8	nd	nd	14.42	7.537

Unit: Corona voltage, V; Corona time, s; Surface temperature, ^{0}C; Surface humidity, %RH; Surface voltage, V; 1/e time, s; 10% cut-off time, s; Surface charge, nC, nd: not defined

Electrostatic Discharge Behavior of the J-AP-Doped PP Blends

The ESD curves of the PP blends doped with J-AP polymer at different ratios are given in **Fig.s 10-12**. With the help of these curves and from the values obtained as a result of the necessary measurements, the usability of the J-AP polymer as an ESD material for each blend was investigated.

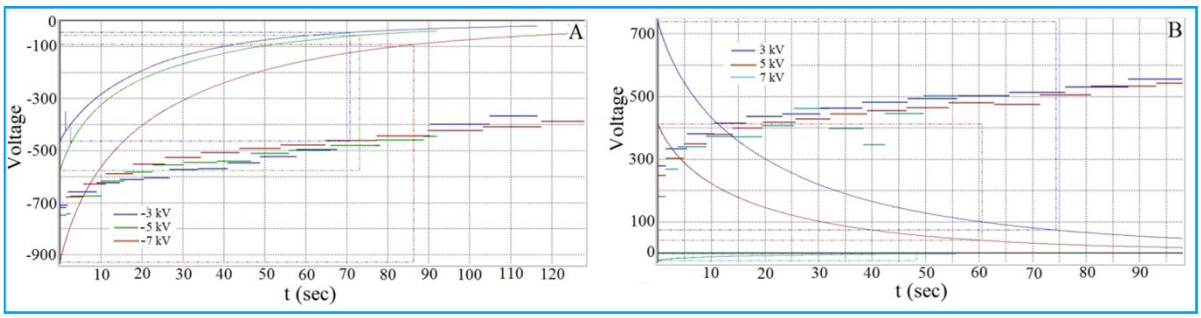


Fig. 10. Electrostatic discharge curves of the $PJ_{0.5}$ blend at corona voltages of -3, -5, and -7 kV (A), and 3, 5, and 7 kV (B).

Fig. 10 shows the ESD curves of the $PJ_{0.5}$ blend at -3, -5 and -7 kV and 3, 5 and 7 kV corona voltages. The results obtained from here and the necessary measurements are summarized in **Table 3**. **Table 3** shows that the surface of the $PJ_{0.5}$ blend accepts quite high voltage values at negative and positive high polarizations. Along with this, $PJ_{0.5}$ showed 1/e and/or 10% cutoff values that can be considered good at both positive and negative low polarizations and positive and negative high polarizations. This means that the $PJ_{0.5}$ blend is quite resistant as an ESD material at positive and negative high and low polarizations and, although it cannot fully provide the criteria in question, because it is resistant against polarization changes, it can be predicted that the J-AP polymer provides ESD protection for the $PJ_{0.5}$ blend. Along with this, this protection is not at a perfect level.

Table 3. ESD values of the $PJ_{0.5}$ blend at different corona voltages.

Corona voltage	Corona time	Surface humidity	Surface temperature	Surface voltage	1/e time	%10 Cut-off time	Surface charge	Capacitance
-7000	0.030	30.0	30.3	-933.5	25.963	86.338	-36.23	16.67
-5000	0.030	30.7	30.4	-585.0	21.963	73.088	-14.27	10.48
-3000	0.011	30.3	30.3	-465.4	23.400	70.838	-1.34	1.98
3000	0.008	30.7	29.8	-27.28	16.088	48.276	1.46	2.31
5000	0.030	30.4	29.6	420.7	18.963	60.526	5.47	5.58
7000	0.030	30.4	30.1	746.8	23.213	74.338	16.94	9.74

Unit: Corona voltage, V; Corona time, s; Surface temperature, ^{0}C; Surface humidity, %RH; Surface voltage, V; 1/e time, s; 10% cut-off time, s; Surface charge, nC

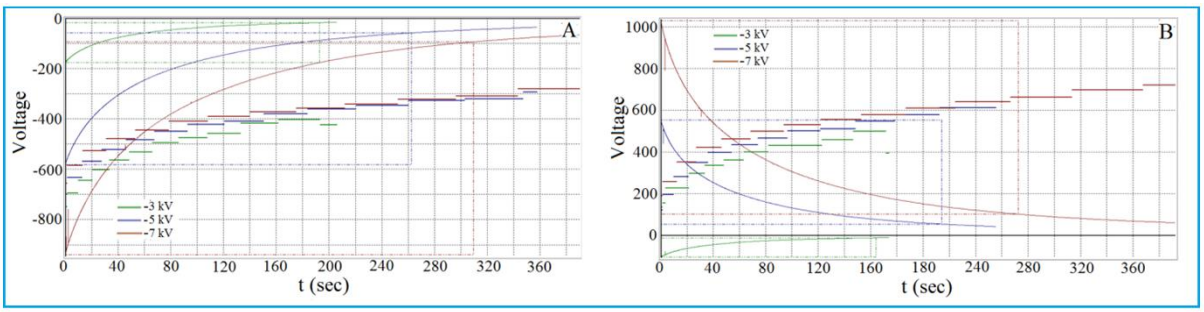


Fig. 11. Electrostatic discharge curves of the PJ_1 blend at corona voltages of -3, -5, and -7 kV (A), and 3, 5, and 7 kV (B).

Fig. 11 illustrates the electrostatic discharge curves of the PJ_1 blend under applied corona voltages of -3, -5, and -7 kV, as well as 3, 5, and 7 kV. The quantitative results derived from these profiles and the requisite measurements are summarized in **Table 4**. **Table 4** shows that the surface of the PJ_1 blend accepts quite high voltage values at negative and positive high polarizations. Nevertheless, the PJ_1 blend exhibited high 1/e and/or 10% decay values across both low and high polarizations, regardless of polarity. Furthermore, **Table 4** reveals that the PJ_1 blend demonstrates considerable resistance as an ESD material against both positive and negative, high and low polarizations. Consequently, this protection is not at an optimal level. Moreover, although it exhibits resistance to polarization fluctuations, its failure to fully satisfy the stringent ESD criteria implies that the J-AP polymer may not reliably provide adequate ESD protection for the PJ_1 formulation.

Table 4. ESD values of the PJ_1 blend at different corona voltages.

Corona voltage	Corona time	Surface humidity	Surface temperature	Surface voltage	1/e time	%10 Cut-off time	Surface charge	Capacitance
-7000	0.030	30.4	30.0	-944.0	92.563	309.463	36.63	16.67
-5000	0.030	30.4	28.8	-584.8	74.588	262.46	14.35	10.55
-3000	0.008	30.4	29.5	-183.5	52.276	192.71	1.716	4.01
3000	0.008	30.4	28.5	-102.9	48.776	164.21	1.237	3.62
5000	0.030	30.1	29.1	560.1	58.026	214.21	10.06	8.25
7000	0.030	30.3	28.8	1033.9	75.338	272.46	18.94	7.92

Unit: Corona voltage, V; Corona time, s; Surface temperature, ^{0}C; Surface humidity, %RH; Surface voltage, V; 1/e time, s; 10% cut-off time, s; Surface charge, nC

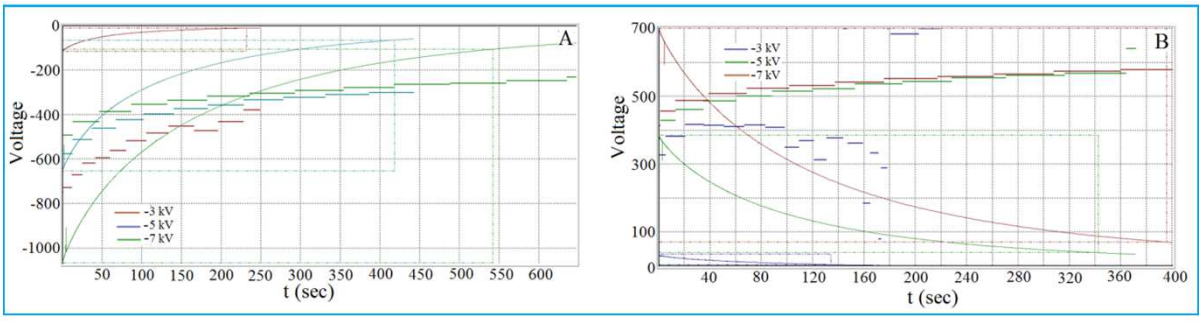


Fig. 12. Electrostatic discharge curves of the PJ_3 blend under applied corona voltages of -3, -5, and -7 kV (A), and 3, 5, and 7 kV (B).

Fig. 12 illustrates the electrostatic discharge curves of the PJ_3 blend under applied corona voltages of -3, -5, and -7 kV, as well as 3, 5, and 7 kV. The quantitative results derived from these profiles and the requisite measurements are summarized in **Table**

5. Table 5 indicates that the surface of the PJ_3 blend accommodates substantially high voltage values under both negative and positive elevated polarizations. Nevertheless, the PJ_3 blend exhibited considerably high 1/e and/or 10% decay values across both low and high polarizations, regardless of polarity. Furthermore, **Table 5** reveals that the PJ_3 blend demonstrates considerable resistance as an ESD material against both positive and negative, high and low polarizations. However, this protection is not at an optimal level. Moreover, despite its resistance to polarization fluctuations, its failure to fully satisfy the stringent ESD criteria implies that the J-AP polymer may not reliably provide adequate ESD protection for the PJ_3 formulation.

Table 5. ESD values of the PJ_3 blend at different corona voltages.

Corona voltage	Corona time	Surface humidity	Surface temperature	Surface voltage	1/e time	%10 Cut-off time	Surface charge	Capacitance
-7000	0.030	30.4	30.0	-1069.4	180.21	541.96	-24.78	9.96
-5000	0.030	30.4	28.7	-657.8	130.71	418.46	-10.13	6.62
-3000	0.008	30.4	29.5	-115.1	65.838	232.24	-1.856	6.37
3000	0.008	30.4	28.4	56.77	56.776	134.32	1.357	3.71
5000	0.030	30.1	29.1	560.1	110.33	343.46	6.40	7.07
7000	0.030	30.3	28.4	1033.9	130.71	395.96	18.40	11.27

Unit: Corona voltage, V; Corona time, s; Surface temperature, ^{0}C; Surface humidity, %RH; Surface voltage, V; 1/e time, s; 10% cut-off time, s; Surface charge, nC

As a result, very good ESD performance could not be obtained from the PJ_n blends obtained by adding the target material J-AP polymer into neat PP at negative and positive low and high polarization values. Therefore, it may not be predicted that the J-AP polymer is generally a suitable ESD material for neat PP except for the $PJ_{0.5}$ blend

Kinetic Analysis

Fundamental Kinetic Equations

The thermal degradation kinetics of neat PP and its J-AP-modified blends were evaluated using six methods based on measurements performed at multiple heating rates. The Kissinger and Kim-Park methods provide apparent activation energies from the temperatures associated with the maximum degradation rate. In contrast, the Tang, KAS, FWO, and Friedman methods evaluate the activation energy at a constant extent of conversion, allowing its variation throughout the degradation process to be examined. Applying these methods together provides a basis for comparing peak-based activation energies with conversion-dependent values.

Kissinger Method

The Kissinger method is a linear, non-isoconversional method used to estimate the apparent activation energy, E, from the temperatures corresponding to the maximum reaction or

decomposition rate. These peak temperatures are obtained from DTG measurements conducted at different heating rates. For the present degradation analysis, T_m represents the absolute temperature at the maximum mass-loss rate in the DTG curve.

The method relates the shift in the peak temperature with heating rate to the temperature dependence of the reaction rate. The commonly used simplified Kissinger equation is expressed as:

$$ln(\frac{\beta}{T_m{}^2}) = ln(\frac{AR}{E}) - \frac{E}{RT_m} \quad (1)$$

The values of $\ln(\beta/T_m^2)$ obtained at different heating rates are plotted against $1/T_m$. The slope of the resulting straight line is -E/R.

Kim-Park Method

The Kim-Park method is a multiple-heating-rate approach used to estimate the apparent activation energy from the peak temperatures corresponding to the maximum decomposition rates. As with the Kissinger method, the analysis uses DTG curves recorded at different heating rates. Its application assumes that the extent of conversion at the maximum degradation rate remains approximately constant across the measurements.

The logarithmic Kim-Park relationship can be written in the following linear form:

$$ln(\beta) = C_{KP} - 1.0516\frac{E}{RT_m} \quad (2)$$

Here, C_{kp} represents the intercept containing the terms associated with the pre-exponential factor, activation energy, and reaction-model parameters under the assumptions of the method. The lnβ values obtained at different heating rates are plotted against $1/T_m$. The slope of the resulting straight line is -1.0516E/R.

Tang Method

The Tang method is an integral isoconversional approach used to determine the conversion-dependent activation energy from thermogravimetric measurements performed at different heating rates. Unlike peak-based methods, it uses the temperatures at which the samples reach the same extent of conversion, α. A separate regression is consequently performed for each selected conversion value. The method employs an approximation to the Arrhenius temperature integral. The Tang equation is expressed as:

$$ln\left(\frac{\beta}{T^{1.894661}}\right) = ln\left(\frac{AE}{Rg(\alpha)}\right) + 3.635041 - 1.894661\, ln\, E - 1.001450\frac{E}{RT} \quad (3)$$

At a constant extent of conversion, $\ln(\beta/T^{1.894661})$ is plotted against 1/T, where T is the absolute temperature corresponding to that conversion at each heating rate. The slope is -1.001450E/R.

Kissinger-Akahira-Sunose Method

The KAS method is an integral, model-free isoconversional approach used to evaluate the apparent activation energy at different stages of thermal degradation. It uses TG or suitably converted DSC data collected at multiple heating rates. For each selected conversion, the corresponding temperatures are identified and used to construct a separate linear plot. The fundamental KAS equation is expressed as:

$$ln(\frac{\beta}{T^2}) = ln(\frac{AR}{Eg(\alpha)}) - \frac{E}{RT} \quad (4)$$

At a constant extent of conversion, ln(β/T²) is plotted against 1/T. The slope of each straight line is −E/R, and the corresponding activation energy is calculated as E = −R × slope.

Although g(α) appears in the intercept, a specific reaction model does not need to be selected to determine the activation energy from the slope at fixed conversion. The KAS method therefore allows the evolution of the apparent activation energy to be examined without assigning a degradation model in advance. Its results can be compared with those obtained using the Tang and FWO methods to assess the influence of the different temperature-integral approximations.

Flynn-Wall-Ozawa Method

The FWO method is an integral, model-free isoconversional method used to determine the conversion-dependent activation energy from thermal analysis data recorded at different heating rates. It is based on the Doyle approximation to the Arrhenius temperature integral. At each selected extent of conversion, the corresponding temperatures from the different heating-rate experiments are used to calculate a separate activation energy. The FWO equation is expressed as:

$$log\ \beta = log(\frac{AE}{Rg(\alpha)}) - 2.315 - 0.4567\frac{E}{RT} \quad (5)$$

At each constant extent of conversion, logβ is plotted against 1/T. The slope of the resulting straight line is -0.4567E/R, and the activation energy is calculated as E = −R × slope/0.4567.

As with the other integral isoconversional methods, the reaction model need not be specified to obtain the activation energy from the slope. The calculated values nevertheless depend on the approximation used for the temperature integral. Comparing the FWO results with the KAS and Tang estimates helps evaluate the consistency of the conversion-dependent kinetic analysis.

Friedman Method

The Friedman method is a differential, model-free isoconversional approach used to determine the apparent activation energy from the conversion rate at a fixed extent of conversion. Whereas the Tang, KAS, and FWO methods use integral relationships, the Friedman method directly applies the differential rate equation. It can be used with TG/DTG data for which conversion and conversion rate have been appropriately defined. Under a constant heating rate, the conversion rate is related to the temperature derivative by dα/dt = β(dα/dT). The Friedman equation is expressed as:

$$ln[\beta(\frac{d\alpha}{dT})] = ln[Af(\alpha)] - \frac{E}{RT} \quad (6)$$

At each constant extent of conversion, ln[β(dα/dT)] is plotted against 1/T. The slope of the resulting straight line is −E/R.

Here, β, T_m, A, E, R, n, α, f(α), and g(α) represent the linear heating rate, the absolute temperature corresponding to the maximum decomposition rate, the Arrhenius pre-exponential factor, the apparent activation energy, the universal gas constant, the apparent reaction order where an nth-order model is employed, the extent of conversion, the differential reaction-model function, and the integral reaction-model function, respectively.

Thermal Degradation Process of J-AP-Doped PP Blends

In this study, the solid-state degradation kinetics of neat PP and its J-AP blends were evaluated using several methods based on multiple heating rates, including Kissinger **[19]**, Kim-Park **[20]**, Tang **[21]**, KAS **[22]**, FWO **[23]**, and Friedman **[24]**. Thermogravimetric (TG) data collected at different heating rates were used to characterize the degradation kinetics. The kinetic analyses were performed using the corresponding TG or derivative thermogravimetric (DTG) curves, allowing the apparent activation energies to be estimated without assuming a specific reaction model in advance. The solid-state degradation mechanisms were subsequently assessed by comparing experimental master plots with theoretical reaction-model curves

The TG/DTG-DTA curves of the neat PP were recorded under dynamic conditions in a nitrogen atmosphere at various heating rates of 5, 10, 15, and 20 °C min^{-1}. **Fig. 13** presents the TG/DTG-DTA curves of the neat PP acquired at these different heating rates. From these curves, which exhibit a single-step degradation process, the onset and final degradation temperatures, as well as the temperatures corresponding to the maximum degradation rate and the respective mass loss percentages, were determined. Furthermore, the TG curves revealed that the onset degradation

temperatures shifted to higher values with an increase in the heating rate. Concurrently, an increase in the residual carbon char yield resulting from the degradation process was observed as the heating rate increased

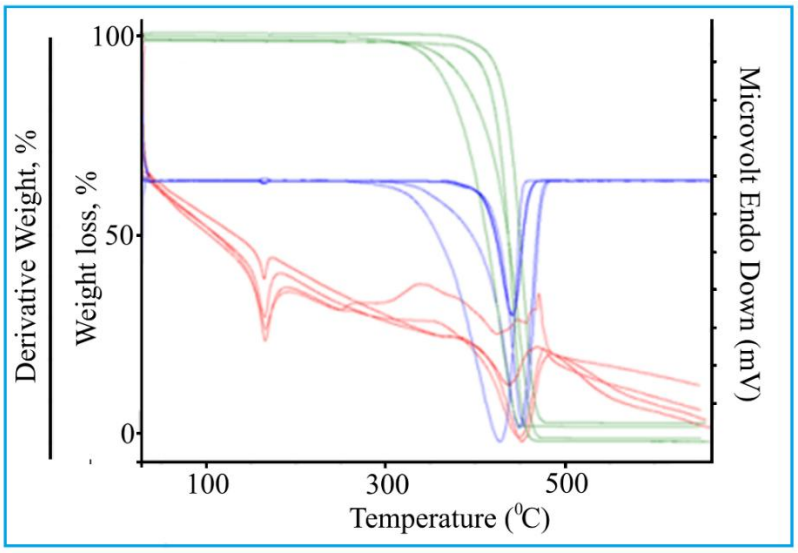


Fig. 13. TG/DTG and DTA curves of neat PP at different heating rates (5, 10, 15 and 20 °C min^{-1}).

For the thermal degradation step, the temperature values corresponding to the highest degradation rate from the related DTG curves of neat PP were measured as 430, 442, 449 and 458 °C. As seen from the curve, the curves shift to high temperature values with increasing heating rate. In the calculation of the kinetic parameters belonging to the thermal degradation of neat PP, firstly the Kissinger, Kim-Park and isoconversional methods, which are independent of the reaction mechanism, were used. The activation energy values related to the solid state degradation kinetics of neat PP were found as 203.83 and 215.74 kJ mol^{-1} according to the Kissinger and Kim-Park method.

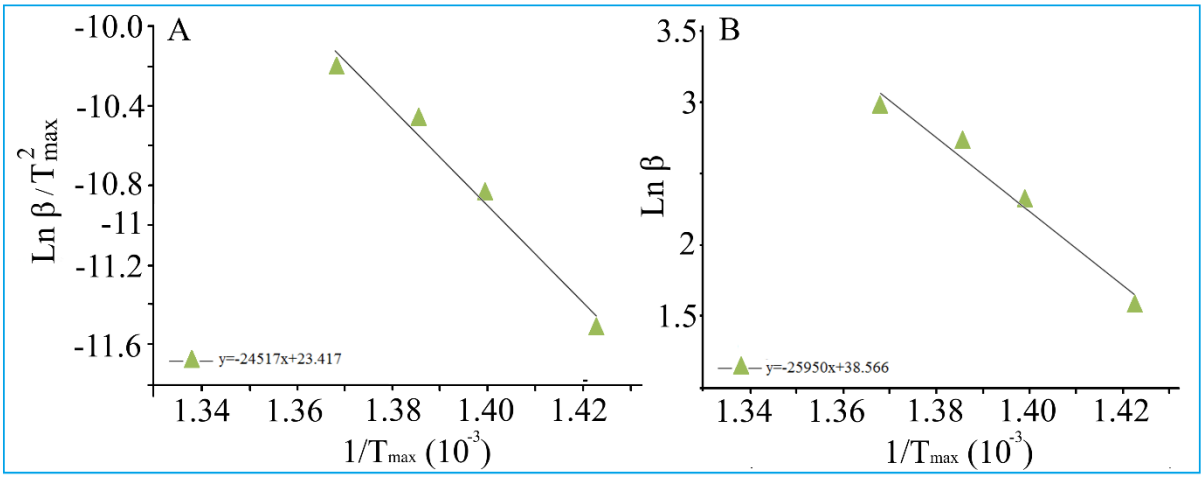


Fig. 14. Kissinger (A) and Kim-Park (B) curves obtained from experimental data for PP at different heating rates.

In **Fig. 14**, the Kissinger and Kim-Park curves obtained from experimental data for neat PP are given. According to the Tang method, the activation energy can be calculated from the plot of ln ($\beta/T^{1.894661}$) versus 1000/T. From the TG curves taken in a nitrogen atmosphere, the average activation energies belonging to the degradation step of the neat PP polymer were found as 192.18 kJ mol^{-1} via the use of the related equation. Another method used in this study is the KAS method. The activation energy from the slopes of the graph of ln(β/T^2) against 1000/T at conversion fractions given as α = 0.05-0.95 was calculated as 193.71 kJ mol^{-1} for the degradation steps of the PP polymer. It was seen that these results are quite close to the values found with the Tang method. Another method used in this study is that of FWO. At constant conversion values, the slopes of the straight lines obtained from the graph of log β against 1000/T become equal to 0.456E/RT. From here, activation energies can be found. The average activation energy values found from the graph of ln *β* against 1000/T at different conversion values for the PP polymer is 193.99 kJ mol^{-1}. Also finally, using the Friedman method which is a differential method, the average activation energy of the PP polymer was calculated as 198.32 kJ mol^{-1}. As a result, the activation energy values related to the solid state degradation kinetics of the PP polymer were determined as 203.83, 215.74, 192.18, 193.71, 193.99 and 198.32 kJ mol^{-1} in the worked conversion fraction limits via the Kissinger, Kim-Park, Tang, KAS, FWO and Friedman methods. All values obtained were presented in **Table 6**. Also, it was found that the degradation functions can be expressed with a single mathematical equation from the changes of the activation energies obtained with the FWO, KAS, Tang and Friedman methods against the conversion fractions at the α=0.05-0.95 limit belonging to the solid state

degradation step of the neat PP polymer. The activation energies required for the degradation step of the PP polymer were determined as quite close to each other between 0.1<α<0.8. The obtained activation energy values related to the solid state degradation kinetics of neat polyolefins were presented in **Table 6**.

Table 6. Activation energy values associated with the solid-state decomposition kinetics of the neat PP

Polymer	Solid state thermal decomposition step						
	Conversion fraction, α	$E_{Kissinger}$	$E_{Kim\text{-}Park}$	E_{Tang}	E_{KAS}	E_{FWO}	$E_{Friedman}$
PP	0.05-0.95	203.83	215.74	192.18	193.71	193.99	198.32

Unit of E- kJ mol^{-1}

Fig. 15 presents the TG/DTG-DTA curves of the PP blends doped with the J-AP polymer, acquired at various heating rates. A single degradation step was consistently observed across the PJ_n blends. Furthermore, it was established that the onset degradation temperatures shifted toward higher values as the heating rate increased. All acquired curves were found to exhibit similar thermal characteristics. For the thermal degradation step, the temperatures corresponding to the maximum degradation rate, derived from the respective DTG curves of the PJ_n blends, were measured as 438, 448, 455, and 461 °C for the $PJ_{0.5}$ blend; 439, 451, 456, and 462 °C for the PJ_1 blend; and 440, 453, 457, and 462 °C for the PJ_3 blend. Accordingly, it was confirmed that the thermal profiles shifted toward higher temperature regions in response to the increasing heating rates.

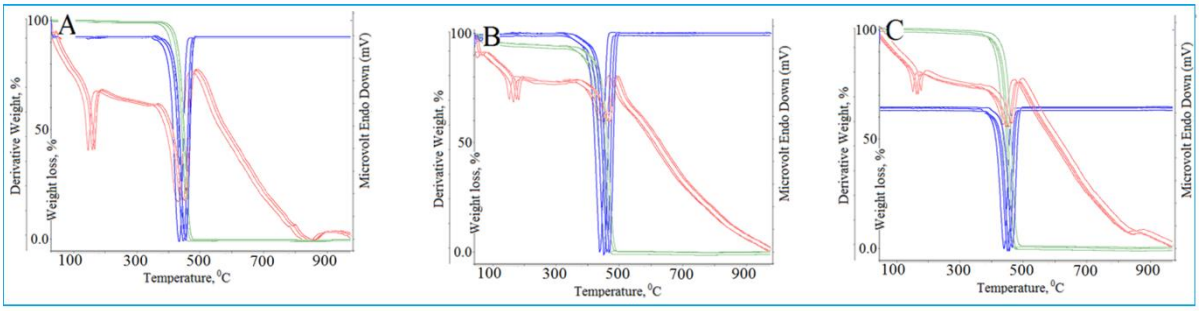


Fig. 15. TG/DTG and DTA curves of $PJ_{0.5}$ (A), PJ_1 (B), and PJ_3 (C) blends at various heating rates.

The Kissinger, Kim-Park, Tang, KAS, FWO, and Friedman methods were employed to calculate the kinetic parameters associated with the thermal degradation of the PP blends doped with the J-AP polymer. **Fig. 16** presents the Kissinger and Kim-Park plots derived from the experimental data for the PJ_n blends.

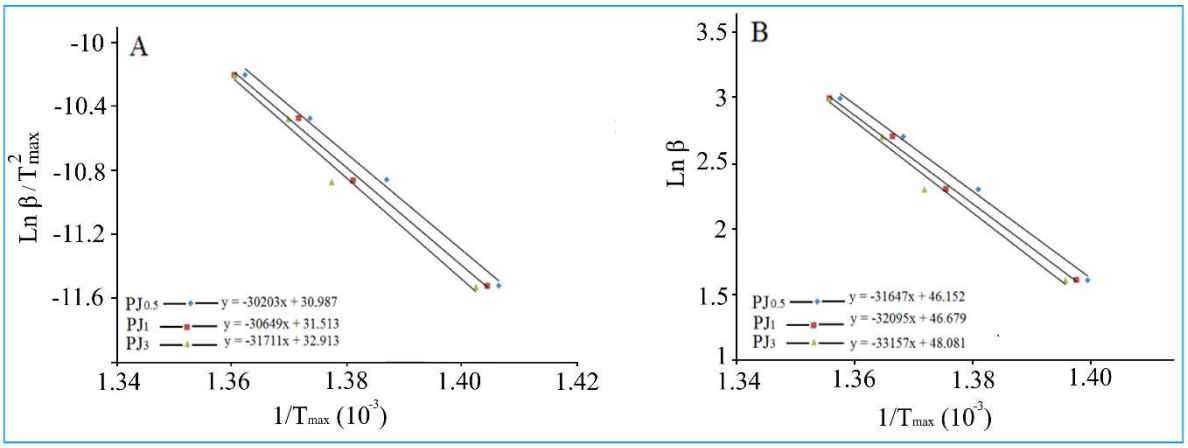


Fig. 16. Kissinger (A) and Kim-Park (B) curves obtained from experimental data for $PJ_{0.5}$, PJ_1 and PJ_3 blends at different heating rates.

The activation energy values associated with the solid-state degradation kinetics of the PJ_n blends, determined via the Kissinger, Kim-Park, Tang, KAS, FWO, and Friedman methods within the conversion range of $0.1<\alpha<0.85$, were found to be 251.10, 263.11, 219.85, 219.63, 220.28, and 223.16 kJ mol^{-1} for the $PJ_{0.5}$ blend; 254.81, 266.83, 227.28, 228.31, 230.82, and 230.83 kJ mol^{-1} for the PJ_1 blend; and 263.64, 275.66, 241.47, 240.23, 243.21, and 244.42 kJ mol^{-1} for the PJ_3 blend, respectively. Based on these findings, an increase of approximately 45-50 kJ mol^{-1} was observed in the activation energy values corresponding to the solid-state degradation kinetics across all PJ_n blends (**Table 7**).

Table 7. Activation energy values associated with the solid-state decomposition kinetics of PJ_n blends

Blend	Solid state thermal decomposition step						
	Conversion fraction, α	$E_{Kissinger}$	$E_{Kim-Park}$	E_{Tang}	E_{KAS}	E_{FWO}	$E_{Friedman}$
$PJ_{0.5}$	0.1-0.85	251.10	263.11	219.85	219.63	220.28	223.16
PJ_1	0.1-0.85	254.81	266.83	227.28	228.31	230.82	230.83
PJ_3	0.1-0.90	263.64	275.66	241.47	240.23	243.21	244.42

The unit of E is kJ mol^{-1}

Solid-State Thermal Degradation Mechanisms of PP and Its J-AP-Modified Blends

In addition to the activation energy values reported in previous section for the thermal degradation reactions of neat polyolefins and their corresponding blends, the solid-state thermal degradation mechanisms were investigated using the master plot method. Master plots were constructed by comparing values derived from experimental data with theoretical predictions. Master plots were constructed by comparing normalized values derived from the experimental thermogravimetric data with the theoretical curves of the solid-state reaction models presented in **Table 8**. These models include diffusion-controlled, nucleation and growth, phase-boundary-

controlled, and reaction-order mechanisms. Each model describes a different dependence of the degradation rate on the degree of conversion (α), providing a basis for distinguishing possible mechanisms governing the thermal decomposition of neat PP and its J-AP-modified blends. The theoretical integral functions, g(α), were normalized to their values at α= 0.5 and plotted as g(α)/g(0.5) against α. The corresponding experimental master plots were then compared with these theoretical curves over the investigated conversion range. The model showing the closest agreement with the experimental curve was considered to provide the most suitable description of the apparent degradation mechanism.

Table 8. Mathematical expressions used in solid-state decomposition processes.

No	Mechanism	Symbol	Differential form, f(α)	Integral form, g(α)
Sigmoidal curves				
1	N and G (n=1)	A_1	$(1- \alpha)$	$[-\ln (1- \alpha)]$
2	N and G (n=1.5)	$A_{1.5}$	$(3/2) (1- \alpha) [-\ln (1- \alpha)]^{1/3}$	$[-\ln (1- \alpha)]^{2/3}$
3	N and G (n=2)	A_2	$2(1- \alpha) [-\ln (1- \alpha)]^{1/2}$	$[-\ln (1- \alpha)]^{1/2}$
4	N and G (n=3)	A_3	$3(1- \alpha) [-\ln (1- \alpha)]^{2/3}$	$[-\ln (1- \alpha)]^{1/3}$
5	N and G (n=4)	A_4	$4(1- \alpha) [-\ln (1- \alpha)]^{3/4}$	$[-\ln (1- \alpha)]^{1/4}$
Deceleration curves				
6	Diffusion, 1D	D_1	$1/ (2\alpha)$	α^2
7	Diffusion, 2D	D_2	$-1/ (\ln (1- \alpha))$	$(1- \alpha)\ln (1- \alpha) + \alpha$
8	Diffusion, 3D	D_3	$1.5/ [(1- \alpha)^{-1/3}-1]$	$(1-2\alpha/3) -(1- \alpha)^{2/3}$
9	Diffusion, 3D	D_4	$[1.5(1- \alpha)^{2/3}] [1-(1- \alpha)^{1/3}]^{-1}$	$[1-(1- \alpha)^{1/3}]^2$
10	Diffusion, 3D	D_5	$(3/2) (1+ \alpha)^{2/3}[(1+ \alpha)^{1/3}-1]^{-1}$	$[(1+ \alpha)^{1/3}-1]^2$
11	Diffusion, 3D	D_6	$(3/2) (1- \alpha)^{4/3}[[1/ (1- \alpha)^{1/3}]-1]^{-1}$	$[[1/ (1- \alpha)]^{1/3}-1]^2$
12	Contracted geometry shape (cylindrical symmetry)	R_2	$2(1- \alpha)^{1/2}$	$1-(1- \alpha)^{1/2}$
13	Contracted geometry shape (sphere symmetry)	R_3	$3(1- \alpha)^{2/3}$	$1-(1- \alpha)^{1/3}$
Acceleration curves				
14	Mample power law	P_1	1	A
15	Mample power law (n=2)	P_2	$2\alpha^{½}$	$\alpha^{1/2}$
16	Mample power law (n=3)	P_3	$3\alpha^{2/3}$	$\alpha^{1/3}$
17	Mample power law (n=4)	P_4	$4\alpha^{3/4}$	$\alpha^{¼}$
18	Mample power law (n=2/3)	$P_{3/2}$	$2/3(\alpha)^{-1/2}$	$\alpha^{3/2}$
19	Mample power law (n=3/2)	$P_{2/3}$	$3/2(\alpha)^{1/3}$	$\alpha^{2/3}$
20	Mample power law (n=4/3)	$P_{3/4}$	$4/3(\alpha)^{1/4}$	$\alpha^{3/4}$

As shown in **Fig. 17**, comparison of the theoretical g(α)/g(0.5) curves as a function of the degree of conversion for the reaction models listed in **Table 8** identified D_3, as the models most closely describing the thermal degradation of neat PP. The corresponding integral reaction functions are $g(\alpha) = (1- 2\alpha/3)- (1- \alpha)^{2/3}$ for D_3. Accordingly, the neat PP exhibited deceleratory behavior. The agreement with these model suggests that degradation begins at the surface and progresses toward the center through a three-dimensional diffusion-controlled mechanism with spherical symmetry.

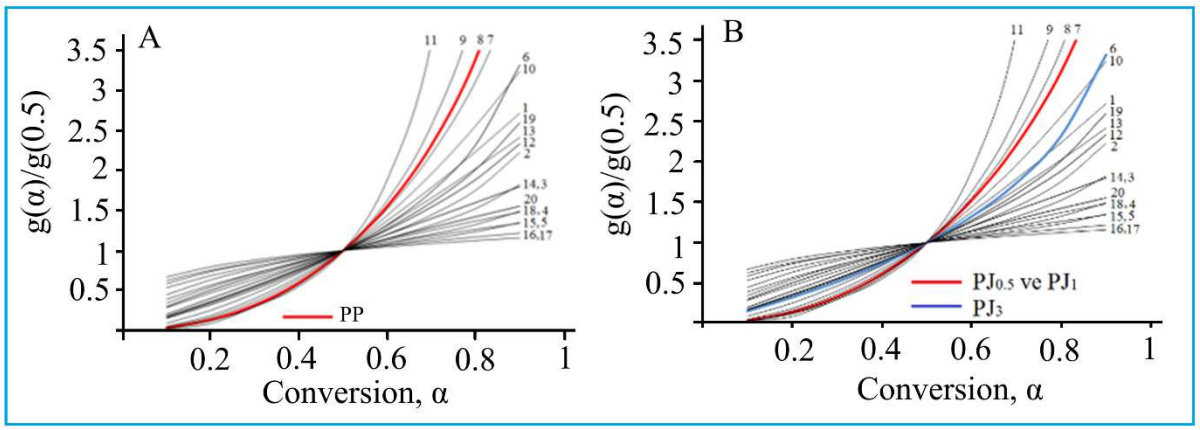


Fig. 17. Comparison of theoretical g(α)/g(0.5) values as a function of the degree of conversion for different reaction models for neat PP and PJ_n blends.

The solid-state thermal degradation mechanisms of the J-AP-modified PP blends were investigated using master plots constructed by comparing experimentally derived values with theoretical predictions. **Fig. 17** presents the master plots describing the solid-state thermal degradation behavior of these blends. The degradation of $PJ_{0.5}$ and PJ_1 was best described by the D_2 model, corresponding to two-dimensional diffusion with the integral reaction function $g(\alpha) = (1-\alpha)\ln(1-\alpha) + \alpha$. For PJ_3, the D_1 model, representing one-dimensional diffusion with $g(\alpha)=\alpha^2$, provided the closest agreement with the experimental data. The inferred progression of diffusion-controlled degradation from the surface toward the center was attributed to the crystallinity of the respective blends. In addition, all blends exhibited deceleratory behavior.

Conclusions

In this study, polypropylene (PP) blends containing 0.5, 1.0, and 3.0 wt% poly(7-amino-4-hydroxy-2-naphthalenesulfonic acid) (J-AP) were prepared. The effects of J-AP loading on the structural, thermal, morphological, mechanical, electrical, and electrostatic charge-dissipation properties of PP were investigated. The incorporation of J-AP into polypropylene produced composition-dependent changes in crystalline organization, thermal stability, mechanical response, fluorescence, and electrostatic charge dissipation. The findings demonstrate that the performance of the blends cannot be evaluated from additive concentration or electrical conductivity alone. Instead, the effects of J-AP must be considered through the relationships among matrix structure, morphology, and the property being targeted.

FTIR-ATR analysis supported the incorporation of J-AP into the PP matrix, while XRD indicated predominantly α-monoclinic crystalline structures in the blends. The DSC-derived crystallinity increased from 34.3% for neat PP to 45.4% for PJ_3, accompanied by an increase in melting temperature from 157.0 to 166.7 °C. These changes suggest that J-AP influences the

crystalline organization of PP during melt processing and subsequent cooling. SEM observations indicated dispersed additive-containing domains, whereas AFM revealed a concentration-dependent surface response. The lower roughness of $PJ_{0.5}$ and PJ_1 relative to neat PP, followed by the higher roughness of PJ_3, shows that additive incorporation does not produce a uniform increase in surface roughness across the composition range.

The thermal analysis provided consistent evidence of enhanced resistance to degradation following J-AP addition. The degradation onset temperature increased from 431 °C for neat PP to 449 °C for PJ_3, while the temperature corresponding to the maximum degradation rate increased from 442 to 453 °C. All compositions retained a predominantly single-step mass-loss profile under the investigated conditions. Thus, J-AP delayed the principal degradation event without introducing a clearly resolved additional mass-loss step. The kinetic results further supported the thermal stabilization observed experimentally. All six methods yielded higher apparent activation energies for the blends than for neat PP. For example, the KAS activation energy increased from 193.71 kJ mol^{-1} for neat PP to 219.63, 228.31, and 240.23 kJ mol^{-1} for $PJ_{0.5}$, PJ_1, and PJ_3, respectively. The agreement in the direction of change across the methods strengthens the conclusion that J-AP alters the effective energy barrier associated with degradation. Master plot comparisons favored the D_2 model for $PJ_{0.5}$ and PJ_1 and the D_1 model for PJ_3.

The mechanical response depended on J-AP loading. PJ3 exhibited the highest elastic modulus (1732.8 MPa), but its elongation at break decreased to 73.58%, compared with 262.18% for neat PP. In contrast, PJ0.5 retained an elongation at break of 268.2%. These findings indicate that the increased stiffness at the highest loading was accompanied by reduced ductility

A central finding is the different concentration dependence of electrical conductivity and charge dissipation. Conductivity increased with J-AP loading, reaching 1.7×10^{-9} S cm^{-1} for PJ3. However, PJ0.5 exhibited the shortest charge-decay times under both positive and negative corona polarization. Increasing the loading to 1.0 or 3.0 wt% prolonged charge decay despite the higher measured conductivity. This behavior indicates that conductivity alone is insufficient to predict dynamic antistatic performance. Changes in interfacial charge trapping, surface morphology, or charge-transport pathways may contribute to this response, but additional measurements are needed to distinguish their contributions.

Overall, J-AP offers a means of modifying several PP properties within a low additive-loading range. PJ3 provided the strongest improvements in thermal stability, stiffness, and visible fluorescence, whereas PJ0.5 showed the most favorable charge-dissipation behavior among the blends. Nevertheless, the measured decay times indicate that effective ESD protection remains

limited under the tested conditions. Future optimization should therefore examine additive distribution, specimen geometry, humidity dependence, and repeated charging behavior alongside conductivity. The results establish that selecting the J-AP loading requires an application-specific balance between thermal-mechanical performance and electrostatic charge dissipation.

Funding

This work was financially supported by the Scientific and Technological Research Council of Turkey (Project Nu.: KBAG-113Z587).

Competing interests

The authors declare no competing interests.

Author contributions

Fatih Doğan: Conceptualization, Data curation, Formal analysis, Investigation, Methodology, Resources, Software, Visualization, Writing-original draft. **Ayşe Nur Özkan:** Data curation, Investigation, Validation, Writing-review & editing. **Kamil Şirin:** Methodology, Resources, Validation, Writing-review & editing. **İsmet Kaya:** Conceptualization, Formal analysis, Funding acquisition, Investigation, Methodology, Project administration, Writing-review & editing.

Data availability

The data supporting the findings of this study are included in the article and its supplementary information files. Additional data are available from the corresponding author upon reasonable request.

Declarations

Conflict of interest

The authors declare that they have no conflict of interest.

Ethical approval

Not applicable.

References

1. Chen Y, Yin Q, Zhang X, Xue X, Jia H. The crystallization behaviors and rheological properties of polypropylene/graphene nanocomposites: The role of surface structure of reduced graphene oxide. Thermochim Acta. 2018;661:124–36. https://doi.org/10.1016/j.tca.2018.01.021

2. Anand A, Rani N, Saxena P, Bhandari H, Dhawan SK. Development of polyaniline/zinc oxide nanocomposite impregnated fabric as an electrostatic charge dissipative material. Polym Int. 2015;64:1096–103. https://doi.org/10.1002/pi.4870

3. Sankaran S, Deshmukh K, Ahamed MB, Khadheer Pasha SK. Recent advances in electromagnetic interference shielding properties of metal and carbon filler reinforced flexible polymer composites: A review. Compos Part A Appl Sci Manuf. 2018;114:49–71. https://doi.org/10.1016/j.compositesa.2018.08.006

4. Zeng Z, Jin H, Chen M, Li W, Zhou L, Zhang Z. Lightweight and Anisotropic Porous MWCNT/WPU Composites for Ultrahigh Performance Electromagnetic Interference Shielding. Adv Funct Mater. 2016;26:303–10. https://doi.org/10.1002/adfm.201503579

5. Zhang H, Zhang G, Gao Q, Zong M, Wang M, Qin J. Electrically electromagnetic interference shielding microcellular composite foams with 3D hierarchical graphene-carbon nanotube hybrids. Compos Part A Appl Sci Manuf. 2020;130:105773. https://doi.org/10.1016/j.compositesa.2020.105773

6. Ganguly S, Bhawal P, Ravindren R, Das NC. Polymer Nanocomposites for Electromagnetic Interference Shielding: A Review. J Nanosci Nanotechnol. 2018;18:7641–69. https://doi.org/10.1166/jnn.2018.15828

7. Mittal G, Dhand V, Rhee KY, Park S-J, Lee WR. A review on carbon nanotubes and graphene as fillers in reinforced polymer nanocomposites. Journal of Industrial and Engineering Chemistry. 2015;21:11–25. https://doi.org/10.1016/j.jiec.2014.03.022

8. Huskić M, Sharma GK, Joseph SL, James NR. Intrinsically conducting polymers and their composites for EMI shielding. Electromagnetic Interference Shielding Materials. Elsevier; 2026. p. 361–405. https://doi.org/10.1016/B978-0-443-36630-7.00011-9

9. Takahashi K, Nagura K, Takamura M, Goto T, Takahashi T. Development of Electrically Conductive Thermosetting Resin Composites through Optimizing the Thermal Doping of Polyaniline and Radical Polymerization Temperature. Polymers (Basel). MDPI; 2022;14. https://doi.org/10.3390/polym14183876

10. da Silva AMG, Barcelos K de A, da Silva MC, Morelli CL. Blend of recycled poly(ethylene terephthalate) and polycarbonate with polyaniline for antistatic packaging. Polymers and Polymer Composites. SAGE Publications Ltd; 2020;28:331–7. https://doi.org/10.1177/0967391119874994

11. Mohsin MEA, Elias M, Arsad A, Yong KC, Alothman O, Zakaria ZY. Electrical conductivity, thermal, rheological and morphological Characteristics of Grafted Blend of Polypyrole and

Polypropylene. Chem Eng Trans. Italian Association of Chemical Engineering - AIDIC; 2017;56:1375–80. https://doi.org/10.3303/CET1756230

12. Anis A, Alhamidi A, Bashir Z, Alam MA, Al-Zahrani SM. Mouldable Conductive Plastic with Optimised Mechanical Properties. Polymers (Basel). 2024;16:311. https://doi.org/10.3390/polym16030311

13. Bhandari H, Singh S, Choudhary V, Dhawan SK. Conducting films of poly(aniline-co-1-amino- 2-naphthol-4-sulfonic acid) blended with LDPE for its application as antistatic encapsulation material. Polym Adv Technol. 2011;22:1319–28. https://doi.org/10.1002/pat.1612

14. Doğan F, Kaya İ, Temizkan K. Multi-response behavior of aminosulfonaphthole system. J Mol Catal B Enzym. 2016;133:234–45. https://doi.org/10.1016/j.molcatb.2016.09.002

15. Edward P. Moore. Polypropylene Handbook: Polymerization, Characterization, Properties, Processing, Applications. Cincinnati, USA: Hanser/Gardner Publications; 1996.

16. Romankiewicz A, Sterzynski T, Brostow W. Structural characterization of α- and β-nucleated isotactic polypropylene. Polym Int. 2004;53:2086–91. https://doi.org/10.1002/pi.1632

17. Broda J. Polymorphism in polypropylene fibers. J Appl Polym Sci. 2003;89:3364–70. https://doi.org/10.1002/app.12570

18. Gadelmawla ES, Koura MM, Maksoud TMA, Elewa IM, Soliman HH. Roughness parameters. J Mater Process Technol. 2002;123:133–45. https://doi.org/10.1016/S0924-0136(02)00060-2

19. Dilek D, Doğan F, Bilici A, Kaya İ. Oxidative synthesis of a novel polyphenol having pendant Schiff base group: Synthesis, characterization, non-isothermal decomposition kinetics. Thermochim Acta. 2011;518:72–81. https://doi.org/10.1016/j.tca.2011.02.009

20. Doğan F. Thermal decomposition behavior of oligo(4-hydroxyquinoline). Polym Eng Sci. 2014;54:992–1002. https://doi.org/10.1002/pen.23639

21. Kök G, Ay K, Ay E, Doğan F, Kaya İ. Synthesis, characterization and non-isothermal decomposition kinetic of a new galactochloralose based polymer. Carbohydr Polym. 2014;101:324–31. https://doi.org/10.1016/j.carbpol.2013.09.065

22. Doğan F, Şirin K, Kaya İ, Balcan M. The influence of $CaCO_3$ filler component on thermal decomposition process of PP/LDPE/DAP ternary blend. Polym Adv Technol. 2010;21:512–9. https://doi.org/10.1002/pat.1461

23. Doğan F, Kaya İ, Bilici A, Yıldırım M. Chemical oxidative polymerization, optical, electrochemical and kinetic studies of 8-amino-2-naphthol. Journal of Polymer Research. 2015;22:104. https://doi.org/10.1007/s10965-015-0737-z

24. Doğan F, Topallar H, Kaya İ, Yürekli M. The effect of the oxidant used during polymerization on the solid-state decomposition kinetics of poly(4-methyl catechol). J Therm Anal Calorim. 2013;111:1515–22. https://doi.org/10.1007/s10973-012-2517-x